LETTERS

# Gelation of particles with short-range attraction

Peter J. Lu[1], Emanuela Zaccarelli[3,4], Fabio Ciulla[3], Andrew B. Schofield[5], Francesco Sciortino[3,4] & David A. Weitz[1,2]

**Nanoscale or colloidal particles are important in many realms of science and technology. They can dramatically change the properties of materials, imparting solid-like behaviour to a wide variety of complex fluids[1,2]. This behaviour arises when particles aggregate to form mesoscopic clusters and networks. The essential component leading to aggregation is an interparticle attraction, which can be generated by many physical and chemical mechanisms. In the limit of irreversible aggregation, infinitely strong interparticle bonds lead to diffusion-limited cluster aggregation[3] (DLCA). This is understood as a purely kinetic phenomenon that can form solid-like gels at arbitrarily low particle volume fraction[4,5]. Far more important technologically are systems with weaker attractions, where gel formation requires higher volume fractions. Numerous scenarios for gelation have been proposed, including DLCA[6], kinetic or dynamic arrest[4,7–10], phase separation[5,6,11–16], percolation[4,12,17,18] and jamming[8]. No consensus has emerged and, despite its ubiquity and significance, gelation is far from understood—even the location of the gelation phase boundary is not agreed on[5]. Here we report experiments showing that gelation of spherical particles with isotropic, short-range attractions is initiated by spinodal decomposition; this thermodynamic instability triggers the formation of density fluctuations, leading to spanning clusters that dynamically arrest to create a gel. This simple picture of gelation does not depend on microscopic system-specific details, and should thus apply broadly to any particle system with short-range attractions. Our results suggest that gelation—often considered a purely kinetic phenomenon[4,8–10]—is in fact a direct consequence of equilibrium liquid–gas phase separation[5,13–15]. Without exception, we observe gelation in all of our samples predicted by theory and simulation to phase-separate; this suggests that it is phase separation, not percolation[12], that corresponds to gelation in models for attractive spheres.**

Gelation occurs in a wide range of systems where particles attract each other[2,5–8,11,12,15–18]. When this attraction is infinitely strong, particles form permanent bonds and grow as fractal clusters that, in turn, bond irreversibly, and can ultimately span the system as a solid-like gel, even as particle volume fraction $\phi$ tends to zero (refs 4, 5, 12, 19). This DLCA limit occurs in many colloidal systems where the interparticle attraction strength, $U$, is much larger than the thermal energy $k_BT$ (refs 4, 5, 12); examples include gold[3,20], silica[3], polymeric lattices[3,6,19], calcium carbonate[21], alumina[2] and silicon carbide[2]. Because bonds once formed never break, DLCA is governed entirely by diffusion; it has thus been considered a purely kinetic phenomenon[3]. Other mechanisms can cause kinetic arrest at far higher $\phi$ (ref. 5). Above $\phi \approx 0.58$, particles can arrest because of crowding to form repulsive glasses, even when $U = 0$; weakly attractive particles can form attractive glasses at lower $\phi$ (ref. 5). Because glasses and DLCA are observed in the same experimental systems, they have been linked within unified pictures of kinetic arrest[4,7,9,10] or jamming[8].

More generally, the onset of gelation can be parameterized by three quantities, namely $\phi$, $U/k_BT$ and $\xi$. The last is the range of the attractive potential in units of $a$, the particle radius[4,22]. These three parameters define a three-dimensional state diagram in which a gelation surface demarcates the well-defined boundary between liquid-like and solid-like behaviour. Many important attraction mechanisms that drive gelation are short-range ($\xi < 0.1$), including van der Waals forces[8,16,21], surface chemistry[2,17,18], hydrophobic effects[7] and some depletion interactions[9,15,23]. Numerous explanations have been advanced for gelation in this small-$\xi$ limit to predict the fluid–solid boundary in the $U$–$\phi$ plane. Non-equilibrium, kinetics-based models have extended the DLCA model to lower $U/k_BT$ by treating bond breakage probabilistically[6,12,20]; have connected the gelation boundary to the percolation threshold[4,12,17,18]; and have extended the glass transition to lower $\phi$ with mode-coupling theory applied to local arrest of individual particles[9], to arrest of clusters[4], and in concert with microscopic modelling of the interparticle attractive potential[23]. Thermodynamic models consider gelation initiated by fluid–crystal[11], liquid–gas[6,14,15], or polymer-like 'viscoelastic'[16] phase separation, which may arrest owing to percolation[12] or a glass transition[4]. These models make strikingly disparate predictions: there is no agreement on either the gelation mechanism, or the location of the gelation boundary[5,12,23].

Here we explore gelation experimentally with a widely-used model colloid–polymer system[6,11,22], where $U/k_BT$ and $\xi$ are controlled by the polymer size and free-volume concentration $c_p$, but in a fashion that is not precisely known. Fixing $\phi = 0.045 \pm 0.005$ and $\xi = 0.059$, we mix samples at various $c_p$; we summarize the samples studied by plotting their values of $c_p$, normalized by the polymer overlap concentration $c_p^*$, in the phase diagrams shown in Fig. 1a, b. We eliminate gravitational sedimentation on multiple-day timescales by meticulously matching the colloid and solvent densities to within $<10^{-4}$. After breaking up particle aggregates by shearing, we observe sample evolution with a high-speed confocal microscope[24].

We observe two phases. In samples with low $c_p$, below the experimental gelation boundary $c_p^g$, we observe a fluid of many clusters that is stable for days; we show a full three-dimensional image of these clusters in the fluid phase for a sample with $c_p = 3.20 \pm 0.03\ \mathrm{mg\,ml^{-1}}$, the closest fluid-phase value below $c_p^g$, in Fig. 1c and in Supplementary Video 1. By contrast, in samples with $c_p > c_p^g$, particles aggregate immediately into clusters, which in turn form a network that spans the macroscopic sample. This network subsequently arrests to create a gel, which we illustrate for a sample with $c_p = 3.31 \pm 0.03\ \mathrm{mg\,ml^{-1}}$, the closest gel-phase value above $c_p^g$, in Fig. 1d and in Supplementary Video 2. The gel undergoes no major structural rearrangement for days, even though it exchanges particles with a dilute gas, shown in Supplementary Video 3. These phases are separated by a very sharp boundary: the gel and fluid illustrated differ in $c_p$ by only a few per cent. Our observation of only these two dramatically different phases contrasts findings of more complex phase behaviour in non-buoyancy-matched systems, where sedimentation can shift or obscure the observed phase boundaries[6,9,12,15,21].

[1]Department of Physics, [2]SEAS, Harvard University, Cambridge, Massachusetts 02138, USA. [3]Dipartimento di Fisica, [4]CNR-INFM-SOFT, Università di Roma La Sapienza, Piazzale A. Moro 2, 00185 Roma, Italy. [5]The School of Physics, University of Edinburgh, Edinburgh EH9 3JZ, UK.

Locating the gelation boundary in general requires a means to compare among experiments and with theory or simulation, using universal thermodynamic quantities, like $U/k_BT$, instead of system-specific parameters, like $c_p$ (refs 9, 23). Unfortunately, it is impossible to precisely determine $U/k_BT$ from a known $c_p$, even using microscopic models for the potential. Instead, we use the finding that the behaviour of an attractive particle system for $\xi < 0.1$ depends not on the shape of the potential, but only on its reduced second virial coefficient, $B_2^* \equiv (3/8a^3)\int_0^\infty (1-\exp(-U(r)/k_BT))r^2\mathrm{d}r$ (ref. 25). After each fluid sample has reached its long-term steady state, we determine its cluster mass distribution $n(s)$, the fraction of total clusters that contain $s$ particles. We then simulate hard spheres with isotropic short-range attractions at the same $\phi$, determining $n(s)$ for different values of $B_2^*$. For each experimental $n(s)$, we select the closest-matching simulated $n(s)$ using a least-squares minimization. This allows us to associate each $c_p$ with a unique $B_2^*$, with no adjustable parameters. These fits all work remarkably well, irrespective of the interparticle attractive potential shape, so long as the potentials have the same $B_2^*$, as shown in Fig. 2. Identical $n(s)$ are observed for the square-well, generalized Lennard–Jones, and Asakura–Oosawa forms, commonly used for colloid–polymer mixtures[9,23,26], substantiating our $c_p$–$B_2^*$ mapping even though the exact experimental potential shape remains unknown. Measuring $n(s)$ requires only straightforward counting of particle bonds; by contrast, determining $B_2^*$ with similar precision from scattering[18] or radial distribution functions[27] requires far more accurate identification of particle positions.

From $B_2^*$, other thermodynamic quantities can be derived directly, including $k_BT/U$ for different potential forms[25]. Considerable insight

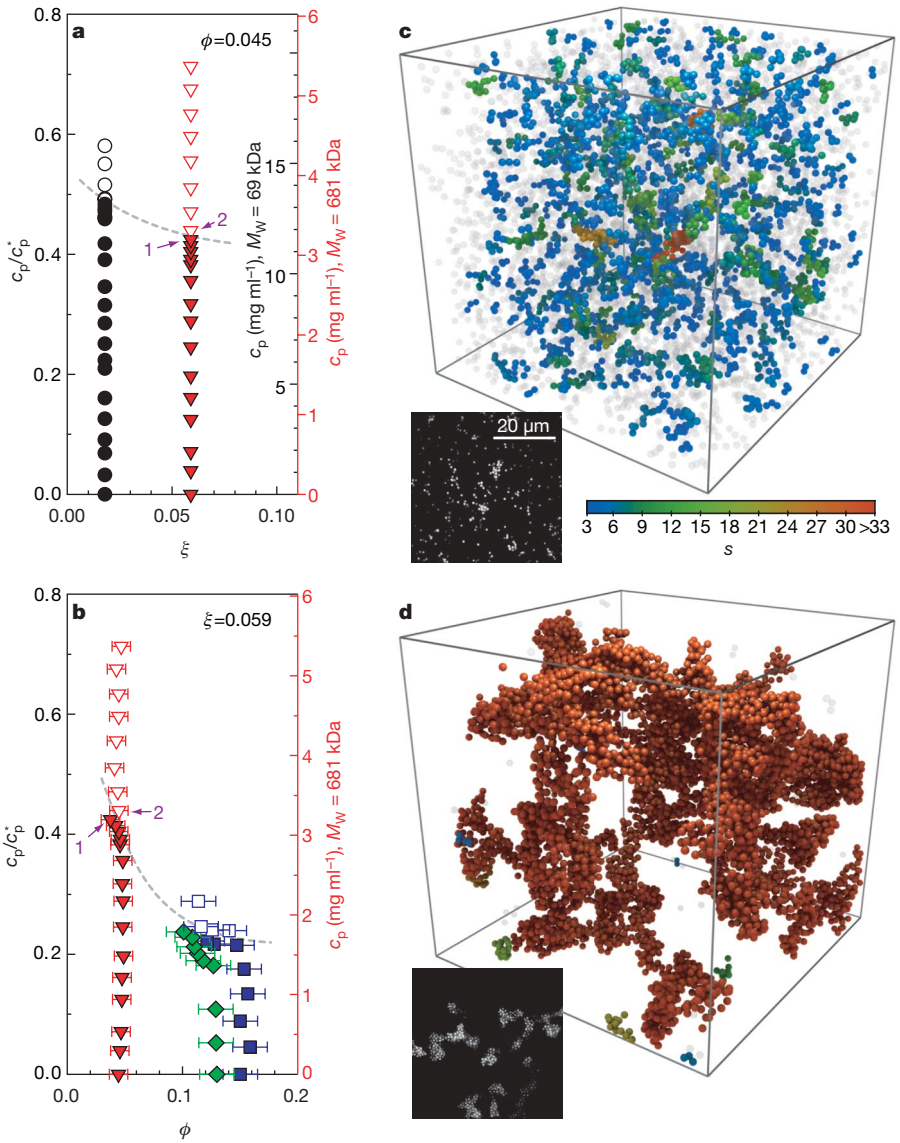


**Figure 1 | Composition and structure of experimental gel and fluid samples.** **a**, Experimental samples in a $c_p/c_p^*$ and $\xi$ phase diagram for constant $\phi = 0.045$. Black circles and red triangles indicate samples with 69 kDa and 681 kDa polystyrene polymers, respectively. Solid symbols mark fluid samples; open symbols, gels. Actual measured $c_p$ values are on secondary vertical axes of the same colour at right. **b**, Experimental samples in a $c_p/c_p^*$ and $\phi$ phase diagram for constant $\xi = 0.059$, with $c_p$ of the 681 kDa polymer used in all samples indicated on the secondary red axis at right. Error bars represent the variation in $\phi$ for different particle configurations from the same sample. In **a** and **b**, dashed grey gelation boundaries are drawn to guide the eye. **c**, 3D reconstruction ($56 \times 56 \times 56\ \mu m^3$), and (inset) single 2D confocal microscope image, for the fluid with the highest $c_p = 3.20\ mg\ ml^{-1}$. The fluid's clusters are coloured by their mass $s$ (number of particles) according to the colour bar, with monomers and dimers rendered in transparent grey to improve visibility. **d**, Reconstruction and confocal image of the gel with the lowest $c_p = 3.31\ mg\ ml^{-1}$ shown at same scale, containing a single spanning cluster. Samples in **c** and **d** are in the long-time steady state four hours after mixing; their compositions are marked in **a** and **b** with the purple numerals 1 and 2, respectively.

is obtained by using $n(s)$ fits to determine the values of $k_BT/U$, calculated for an Asakura–Oosawa potential with $\xi = 0.059$ to match the experiment, and plotting these as a function of $c_p$ for all fluid samples. The data exhibit an unexpected linear dependence near the experimentally determined gelation boundary at $c_p^g = 3.25 \pm 0.05\,\mathrm{mg\,ml^{-1}}$, as shown in Fig. 3a. We calculate the onset of phase separation both in the Baxter model and with simulation, which, in all cases, yield identical results. Remarkably, these correspond precisely to the experimentally determined value of $k_BT/U$ at the gel boundary, as shown in Fig. 3a. This suggests that the gel boundary occurs exactly at the boundary of phase separation. Because the spinodal and binodal lines are very close for all short-range potentials, such as those here, we do not observe nucleation and growth—instead, the observed phase separation is always driven by spinodal decomposition.

To confirm the generality of these results, we repeat the experiment for different $\phi$ and $\xi$. Again fixing $\xi = 0.059$, we create additional samples at $\phi \approx 0.13$ and $\phi \approx 0.16$, as shown in the phase diagram in Fig. 1b. Increasing $\phi$ results in larger clusters, whose mass distribution broadens to more closely resemble a power law, as shown in Fig. 2f; this is reminiscent of an approach to the critical point predicted at $\phi_c \approx 0.27$ (ref. 28). In addition, for $\phi = 0.045$, we also reduce $\xi$ to 0.018; this yields more tenuous, branched, thinner clusters[22]. These samples are shown in the phase diagram in Fig. 1a. In all cases, the experimentally determined value of $k_BT/U$ at the gelation boundary coincides exactly with the theoretical phase separation boundary, as shown in Fig. 3b–d. Finally, we consider the dependence of $B_2^* - 1$, normalized by the value at the phase separation boundary, as a function of $c_p/c_p^g$. Unexpectedly, despite significant variation in cluster morphology, all sample data scale onto a single master curve, shown in Fig. 3e. This highlights the similarities in behaviour of all samples on approach to the spinodal line and points to a universal mechanism for gelation.

These data suggest that, for isotropic short-range interactions, all gelation is triggered by spinodal decomposition, a phase separation process driven by a thermodynamic instability. If this is so, then we should independently observe other characteristics of equilibrium phase separation in samples that form gels. One such feature is the coexistence of gel and colloidal gas: we observe occasional exchange of particles between gas and gel, as shown in Supplementary Video 3;

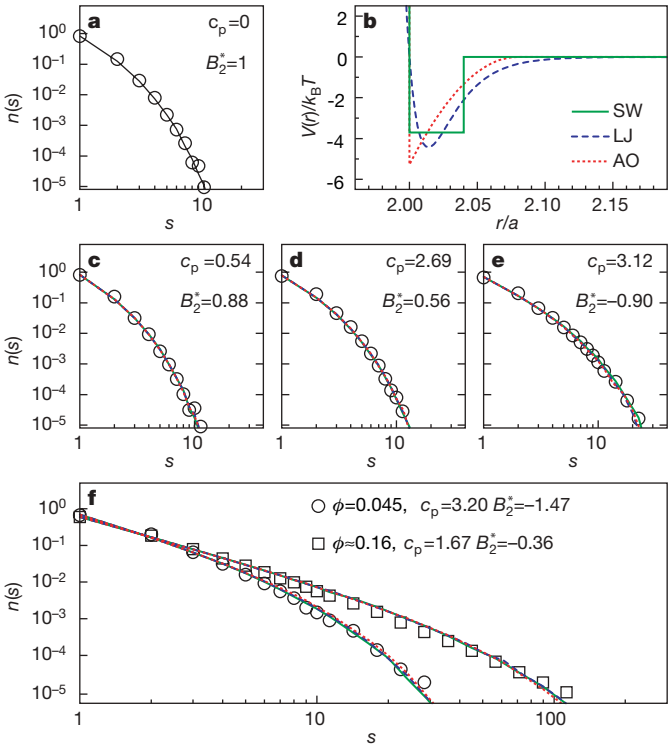


**Figure 2 | Comparisons among cluster mass distributions $n(s)$ for $\xi = 0.059$.** **a**, Comparison at $\phi = 0.045$ between experimental data for $c_p = 0$ (circles), and simulation results for a hard-sphere potential ($U/k_BT = 0$ and $B_2^* = 1$; solid line), demonstrating an exact match. In this and all panels, value of $c_p$ is in $\mathrm{mg\,ml^{-1}}$. **b**, Three potentials at the same $B_2^*$ used to generate $n(s)$ in simulations with finite attractions; solid green, dashed blue and dotted red lines denote square-well (SW), generalized Lennard–Jones (LJ) and Asakura–Oosawa (AO) potentials, respectively. Example potentials shown for $B_2^* = -1.47$. **c–e**, Example comparisons at $\phi = 0.045$ between experimental $n(s)$, marked by circles, and simulation $n(s)$, by lines coloured as the corresponding potentials in **b**. **c**, $c_p = 0.54\,\mathrm{mg\,ml^{-1}}$ and $B_2^* = 0.88$. **d**, $c_p = 2.69\,\mathrm{mg\,ml^{-1}}$ and $B_2^* = 0.56$. **e**, $c_p = 3.12\,\mathrm{mg\,ml^{-1}}$ and $B_2^* = -0.90$. **f**, Comparisons for the fluids with the highest $c_p$ closest to the gel boundary at $c_p^g$. Circles denote the fluid with $\phi = 0.045$ ($c_p = 3.20\,\mathrm{mg\,ml^{-1}}$ and $B_2^* = -1.47$; sample illustrated in Fig. 1c). Squares denote the fluid with $\phi \approx 0.16$ ($c_p = 1.67\,\mathrm{mg\,ml^{-1}}$ and $B_2^* = -0.36$), whose significantly larger clusters are expected as the $\phi_c = 0.27$ critical point is approached. All data sets match exactly, confirming that $n(s)$ both usefully maps experimental to simulation results and does not depend on potential shape.

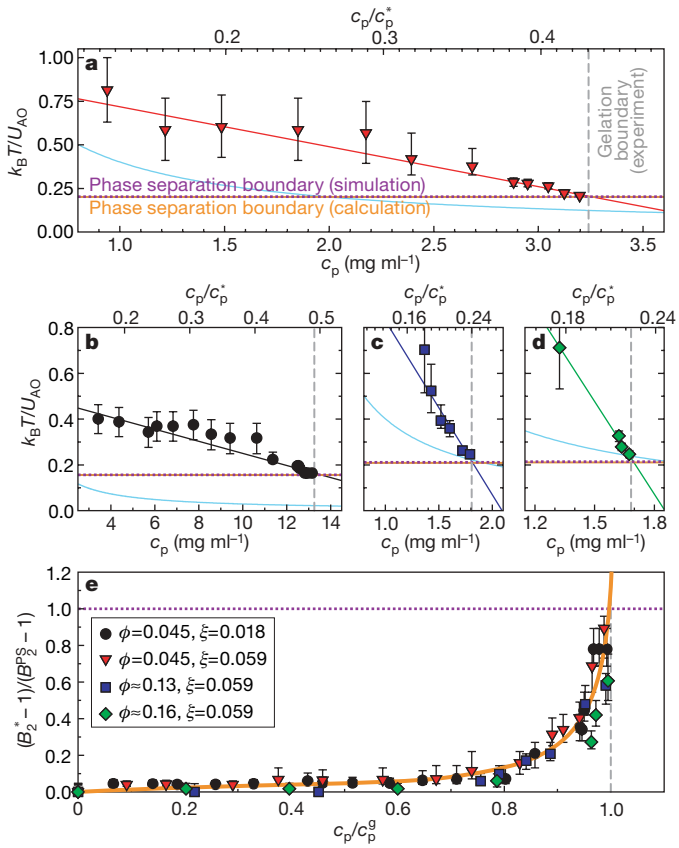


**Figure 3 | Comparison of $n(s)$ mapping of experimental $c_p$ to $k_BT/U$.** Data are shown for **a**, $\phi = 0.045$ and $\xi = 0.059$, **b**, $\phi = 0.045$ and $\xi = 0.018$, **c**, $\phi \approx 0.13$ and $\xi = 0.059$, and **d**, $\phi \approx 0.16$ and $\xi = 0.059$. Grey dashed vertical lines demarcate the experimental gelation boundary at $c_p^g$; horizontal lines demarcate the theoretical phase separation boundary calculated in the Baxter model (orange solid line) and with simulation (purple dotted line), which always coincide. Coloured symbols (as used in Fig. 1a, b and shown in the key in **e**) with best-fit lines represent the results of the $n(s)$ mapping illustrated in Fig. 2; error bars correspond to the uncertainty from the least-squares fitting. The experimental gelation boundary exactly matches the theoretical phase separation boundary for all $\phi$ and $\xi$; by contrast, analytic approximation to the Asakura–Oosawa potential, shown in light blue, does not match at all. **e**, Mapping between $c_p$ and $B_2^* - 1$ for all fluid samples, where $c_p$ is normalized by $c_p^g$ (grey dashed vertical line), and $B_2^* - 1$ by $B_2^{PS} - 1$, its value at the phase separation boundary (purple dotted horizontal line). All data collapse onto a single master curve, highlighted with an orange line to guide the eye. Gelation exhibits universal scaling independent of $\phi$, $\xi$ or shape of the short-range potential.

this is not readily explained by kinetic gelation models based on local arrest[9,10]. An even more distinctive hallmark of spinodal decomposition is the development of a peak in the static structure factor $S(q)$ at finite scattering vector $q$ (refs 19, 29). We again observe this: in fluid samples with $\phi = 0.045$, $\xi = 0.059$ and $c_p < c_p^g$, $S(q)$ shows only a slight rise at low $q$; however, increasing $c_p$ by just a few per cent across $c_p^g$ increases the height of the peak in $S(q)$ by two orders of magnitude, as shown in Fig. 4a. Further distinguishing characteristics of spinodal decomposition occur in the temporal evolution of $S(q)$, where the peak narrows and moves towards lower $q$, and in its first moment $q_1(t)$, which exhibits a power law dependence. Once again, the gel samples unambiguously demonstrate these features: at the earliest times, the peak in $S(q)$ narrows and moves to lower $q$, as shown in Fig. 4b; moreover, $q_1(t)$ scales as $t^{-1/6}$, as shown in Fig. 4c, exactly as in molecular spinodal decomposition[30]. Two hours after mixing, the spinodal decomposition towards the equilibrium phase-separated state is interrupted, as the sample dynamically arrests to form a gel; $S(q)$ and $q_1$ no longer change with time, as shown in Fig. 4b–c. Similar dynamics for $S(q)$ are observed in all gel samples, further demonstrating that liquid–gas spinodal decomposition ubiquitously induces gelation for short-range potentials.

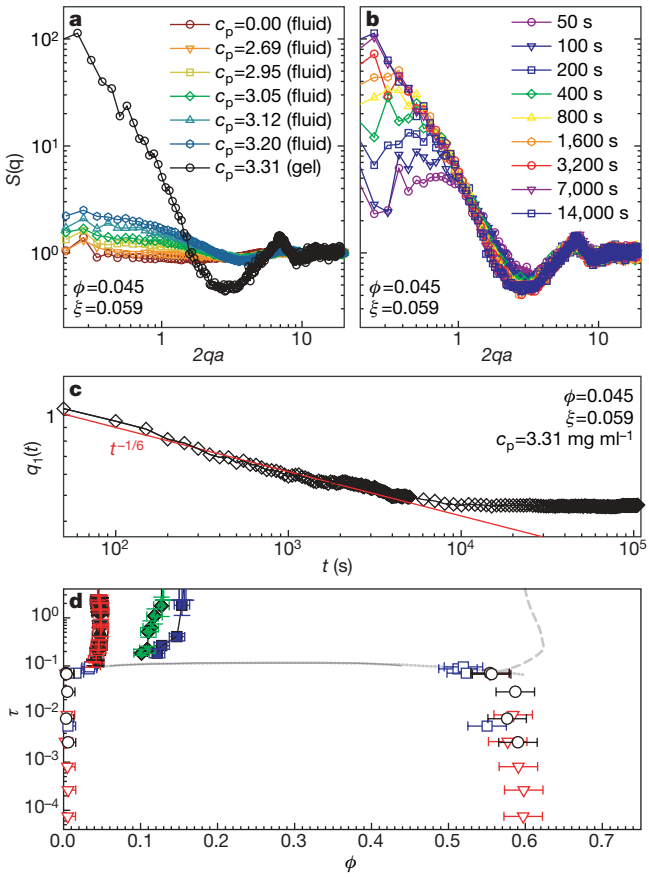


**Figure 4 | Spinodal decomposition in samples that form gels.** **a**, $S(q)$ in the long-time steady-state limit for fluid samples at $\phi = 0.045$ and $\xi = 0.059$ with $c_p \leq 3.20$ mg ml$^{-1}$ (coloured symbols) and the gel sample with $c_p = 3.31$ mg ml$^{-1}$ (black circles). Blue hexagons and black circles denote the fluid and gel samples illustrated in Fig. 1c and d, respectively. All fluid samples show $S(q)$ rising slightly at low $q$ as $c_p \rightarrow c_p^g$. As $c_p$ crosses $c_p^g$ into the gel region, $S(q)$ develops a significant peak two orders of magnitude higher. **b**, Time evolution of $S(q)$ for this gel. Immediately after sample homogenization, a finite-$q$ peak grows, narrows, and shifts to lower $q$, as expected for spinodal decomposition. **c**, $q_1(t)$ (black diamonds) follows a $t^{-1/6}$ power law (red line), another hallmark of spinodal decomposition. After two hours, the sample arrests to form a gel, and $S(q)$ and $q_1$ do not change. **d**, Universal phase diagram of the Baxter parameter $\tau \equiv 1/4(B_2^* - 1)$ and $\phi$ for all samples, with symbols as in Fig. 1a, b and estimates of $\phi$ shown for both gas and gel phases after phase separation. Error bars represent the variation in $\phi$ for different particle configurations from the same sample. All samples predicted to phase-separate within the Baxter model, falling below the theoretical phase separation boundary from ref. 28 (solid grey line), form gels with the same $\phi_g$. Speculative extensions of this boundary (dotted grey line) and of the glass transition (dashed grey line) are plotted to guide the eye.

Together, these results provide strong, quantitative physical evidence that the gelation boundary for short-range attractive particles is precisely equivalent to the boundary for equilibrium liquid–gas phase separation. Gelation requires spinodal decomposition to generate the clusters that span the system and dynamically arrest. Our findings experimentally confirm previous theoretical predictions[5,13,14], and support the suggestion that the ostensibly purely kinetic DLCA regime is in fact a deeply quenched limit of spinodal decomposition[19,29]. Thus, thermodynamic instability appears to drive all gelation of particles with isotropic short-range attractions.

We cannot harmonize our results with predictions from phase separation that is not liquid–gas[11,16], nor from purely kinetic paradigms[4,8–10]. However, the expression of these predictions as system-specific $c_p/c_p^*$ values calculated for the Asakura–Oosawa potential may affect comparison of results. To test this, we plot $k_BT/U$ versus $c_p/c_p^*$ for an analytic approximation to the Asakura–Oosawa potential[9] in Fig. 3a–d, which in all cases dramatically misses the actual potential strength determined from the $n(s)$ mapping; this corroborates previous findings that the Asakura–Oosawa model does not quantitatively describe colloid–polymer mixtures[23,26,27].

Instead, universal system-independent parameters, such as $B_2^*$ (refs 5, 12, 13, 15, 17, 18) and $\phi$, allow meaningfully quantitative comparison between different experiments and with theory. We present such a comparison, as a universal phase diagram for short-range gelation, in Fig. 4d. Without exception, all samples predicted within the Baxter model to phase-separate form gels. This suggests that the gelation line coincides with the phase separation boundary in the Baxter model; other isotropic short-range potentials have similar behaviour. For gel samples, we estimate the volume fractions in both colloidal gas and gel phases by numerically determining the free volume accessible to a test particle of radius $a$; we consider this the total volume of the gas phase, and assign the remaining volume to the gel. Surprisingly, we find the that all spanning gel clusters have $\phi_g \approx 0.55$, independent of both $c_p$ and the average $\phi$ before phase separation. We never observe arrested spanning clusters with significantly lower $\phi_g$; the attractive glass line must therefore intersect the phase separation boundary at $\phi \approx 0.55$ (refs 5, 13), consistent with the origin of kinetic arrest arising from the dense phase undergoing an attractive glass transition[5,13]. Furthermore, $\phi_g$ does not decrease with increasing attraction strength[4,7,9], suggesting that the attractive glass line does not extend into the phase separation region, but instead follows its boundary.

Our results could shed light on non-equilibrium behaviour in technological systems. Even approximate measures of structural parameters, such as $n(s)$, may, when compared with simulations, allow mapping between thermodynamic quantities and experimental parameters when even the rough form of the potential cannot be measured. Moreover, because the onset of non-equilibrium behaviour is in fact governed by equilibrium phase separation, thermodynamic calculations may facilitate quantitative prediction of product stability, a critically important problem in the formulation and manufacture of commercial complex fluids.

## METHODS SUMMARY

We suspend polymethylmethacrylate (PMMA) colloidal spheres of radius $a = 560$ nm in a solvent mixture with matching buoyancy and refractive index, adding an organic salt to screen Coulombic repulsion and linear polystyrene to induce a depletion attraction[22,24]. We determine the radii of colloid and polymer coils with light scattering. We image all samples in a high-speed, automated confocal microscope[24], collecting 181 images at 10 frames per second in each three-dimensional (3D) stack, which occupies a $60 \times 60 \times 60\ \mu m^3$ cube within the sample. We use previously described image-processing software[24] to determine the 3D positions of all colloidal particles in each sample. In total, we collected half a terabyte of image data and located $\sim 10^8$ particles. We use

Pixar's RenderMan (https://renderman.pixar.com) to create 3D reconstructions. We perform simulations of fluid samples of 10,000 particles in a cubic box with periodic boundary conditions for several values of $B_2^*$, using several simulated potentials: a hard-sphere potential, a square-well potential of width $0.04a$, an Asakura–Oosawa potential of maximum width $0.08a$, and a generalized $2\alpha$-$\alpha$ Lennard–Jones potential with exponent $\alpha = 100$. Following a constant-temperature equilibration run, we generate 100 independent realizations in the micro-canonical ensemble for subsequent analysis. We estimate the spinodal line following the temperature-dependence of the energy and of the small angle structure factor within simulations[13], and using the energy route in the Percus–Yevick approximation to the Baxter model for hard spheres with an infinitesimally short attraction range[28]. We use the same procedure in experiment and simulation to assign particles to clusters by considering which particles share common bonds; two particles are considered bonded if they are separated by less than the bond distance $r_b$, fixed by matching the $c_p = 0$ cluster-mass distributions. We use a least-squares minimization to best match numerical distributions to the experimental results with no free parameters.

**Full Methods** and any associated references are available in the online version of the paper at www.nature.com/nature.

**Received 11 December 2007; accepted 14 March 2008.**


1. Mezzenga, R., Schurtenberger, P., Burbidge, A. & Michel, M. Understanding foods as soft materials. *Nature Mater.* **4,** 729–740 (2005).
2. Gauckler, L. J., Graule, Th. & Baader, F. Ceramic forming using enzyme catalyzed reactions. *Mater. Chem. Phys.* **61,** 78–102 (1999).
3. Lin, M. Y. *et al.* Universality in colloid aggregation. *Nature* **339,** 360–362 (1989).
4. Kroy, K., Cates, M. E. & Poon, W. C. K. Cluster mode-coupling approach to weak gelation in attractive colloids. *Phys. Rev. Lett.* **92,** 148302 (2004).
5. Zaccarelli, E. Colloidal gels: Equilibrium and non-equilibrium routes. *J. Phys. Condens. Matter* **19,** 323101 (2007).
6. de Hoog, E. H. A., Kegel, W. K., van Blaaderen, A. & Lekkerkerker, H. N. W. Direct observation of crystallization and aggregation in a phase-separating colloid-polymer suspension. *Phys. Rev. E* **64,** 021407 (2001).
7. Cardinaux, F., Gibaud, T., Stradner, A. & Schurtenberger, P. Interplay between spinodal decomposition and glass formation in proteins exhibiting short-range attractions. *Phys. Rev. Lett.* **99,** 118301 (2007).
8. Trappe, V., Prasad, V., Cipelletti, L., Segre, P. N. & Weitz, D. A. Jamming phase diagram for attractive particles. *Nature* **411,** 772–775 (2001).
9. Bergenholtz, J., Poon, W. C. K. & Fuchs, M. Gelation in model colloid-polymer mixtures. *Langmuir* **19,** 4493–4503 (2003).
10. Puertas, A. M., Fuchs, M. & Cates, M. E. Competition between glass transition and liquid-gas phase separation in attracting colloids. *J. Phys. Condens. Matter* **19,** 205140 (2007).
11. Pusey, P. N., Pirie, A. D. & Poon, W. C. K. Dynamics of colloid-polymer mixtures. *Physica A* **201,** 322–331 (1993).
12. Poon, W. C. K. & Haw, M. D. Mesoscopic structure formation in colloidal aggregation and gelation. *Adv. Colloid Interface Sci.* **73,** 71–126 (1997).
13. Foffi, G., De Michele, C., Sciortino, F. & Tartaglia, P. Scaling of dynamics with the range of interaction in short-range attractive colloids. *Phys. Rev. Lett.* **94,** 078301 (2005).
14. Charbonneau, P. & Reichman, D. R. Systematic characterization of thermodynamic and dynamical phase behavior in systems with short-ranged attraction. *Phys. Rev. E* **75,** 011507 (2007).
15. Buzzaccaro, S., Rusconi, R. & Piazza, R. "Sticky" hard spheres: Equation of state, phase diagram, and metastable gels. *Phys. Rev. Lett.* **99,** 098301 (2007).
16. Tanaka, H., Nishikawa, Y. & Koyama, T. Network-forming phase separation of colloidal suspensions. *J. Phys. Condens. Matter* **17,** L143–L153 (2005).
17. Verduin, H. & Dhont, J. K. G. Phase diagram of a model adhesive hard-sphere dispersion. *J. Colloid Interface Sci.* **172,** 425–437 (1995).
18. Grant, M. C. & Russel, W. B. Volume-fraction dependence of elastic moduli and transition temperatures for colloidal silica gels. *Phys. Rev. E* **47,** 2606–2614 (1993).
19. Carpineti, M. & Giglio, M. Spinodal-type dynamics in fractal aggregation of colloidal clusters. *Phys. Rev. Lett.* **68,** 3327–3330 (1992).
20. Liu, J., Shih, W. Y., Sarikaya, M. & Aksay, I. A. Fractal colloidal aggregates with finite interparticle interactions: Energy dependence of the fractal dimension. *Phys. Rev. A* **41,** 3206–3213 (1990).
21. Allain, C., Cloitre, M. & Wafra, M. Aggregation and sedimentation in colloidal suspensions. *Phys. Rev. Lett.* **74,** 1478–1481 (1995).
22. Lu, P. J., Conrad, J. C., Wyss, H. M., Schofield, A. B. & Weitz, D. A. Fluids of clusters in attractive colloids. *Phys. Rev. Lett.* **96,** 028306 (2006).
23. Shah, S. A., Chen, Y. L., Schweizer, K. S. & Zukoski, C. F. Phase behavior and concentration fluctuations in suspensions of hard spheres and nearly ideal polymers. *J. Chem. Phys.* **118,** 3350–3361 (2003).
24. Lu, P. J., Sims, P. A., Oki, H., Macarthur, J. B. & Weitz, D. A. Target-locking acquisition with real-time confocal (TARC) microscopy. *Opt. Express* **15,** 8702–8712 (2007).
25. Noro, M. G. & Frenkel, D. Extended corresponding-states behavior for particles with variable range attractions. *J. Chem. Phys.* **113,** 2941–2944 (2000).
26. Bolhuis, P. G., Louis, A. A. & Hansen, J.-P. Influence of polymer-excluded volume on the phase-behavior of colloid-polymer mixtures. *Phys. Rev. Lett.* **89,** 128302 (2002).
27. Royall, C. P., Louis, A. A. & Tanaka, H. Measuring colloidal interactions with confocal microscopy. *J. Chem. Phys.* **127,** 044507 (2007).
28. Miller, M. A. & Frenkel, D. Competition of percolation and phase separation in a fluid of adhesive hard spheres. *Phys. Rev. Lett.* **90,** 135702 (2003).
29. Sciortino, F. & Tartaglia, P. Structure factor scaling during irreversible cluster-cluster aggregation. *Phys. Rev. Lett.* **74,** 282–285 (1995).
30. Furukawa, H. A dynamic scaling assumption for phase separation. *Adv. Phys.* **34,** 703–750 (1985).


**Supplementary Information** is linked to the online version of the paper at www.nature.com/nature.

**Acknowledgements** P.J.L. thanks D. Maas, M. Christiansen and S. Raghavachary for assistance in producing the renderings and movies. This work was supported by NASA, the NSF, the Harvard MRSEC, MIUR-Prin and the Marie Curie Research and Training Network on Dynamical Arrested States of Soft Matter and Colloids.

**Author Information** Reprints and permissions information is available at www.nature.com/reprints. Correspondence and requests for materials should be addressed to P.J.L. (plu@fas.harvard.edu).

## METHODS

**Colloid sample preparation.** Following our previously reported procedure[22,24], we equilibrate sterically stabilized colloidal spheres of polymethylmethacrylate (PMMA) with $DiIC_{18}$ fluorescent dye in a 5:1 (by mass) solvent mixture of bromocyclohexane (CXB, Aldrich) and decahydronaphthalene (DHN, Aldrich) for several months. We add tetrabutylammonium chloride (TBAC, Fluke) until saturated (~4 mM) to screen long-range Coulombic repulsion. We then split the colloid suspension to create two stock solutions, adding linear polystyrene (Polymer Labs) depletant polymer to one. We buoyancy-match each stock solution individually by adding either CXB or DHN dropwise until particles remain neutrally buoyant after centrifuging at 1,000*g* for 30 min at 25.0 ± 0.1 °C. Mixing various ratios of the two stock solutions generates samples at varying $c_p$, while maintaining constant $\phi$, TBAC concentration, and buoyancy match.

We determine the radius $a = 560 \pm 10$ nm of our particles with dynamic light scattering[31]. The solvent has viscosity $\eta = 1.96$ mPa s at 25.0 ± 0.1 °C, measured with a Cannon-Fenske viscometer. For the depletant polystyrene, we selected two molecular weights, $M_W = 69.2$ kDa and $M_W = 681$ kDa. From Zimm plots of static light scattering data, we determine the radii of gyration $r_g$ of the two polymers to be 10.0 and 33.0 nm, respectively. This yields $\xi \equiv r_g/a$ of 0.018 and 0.059, respectively, and overlap concentrations $c_p^* \equiv 3M_W/4\pi r_g^3 N_A$ of 27.2 and 7.5 mg ml$^{-1}$, respectively, where $N_A$ is Avogadro's number. In all cases, we directly measure the raw polymer concentrations as a mass ratio of mg polystyrene per g of total sample mass, which we express as a $\phi$-dependent free-volume $c_p$ (mg ml$^{-1}$) according to ref. 32.

**Confocal microscopy.** Following our previously reported imaging protocol[22,24], we load each sample into a glass capillary of internal dimension $50 \times 2 \times 0.1$ mm$^3$ (VitroCom), along with a small piece of magnetic wire with 25 μm diameter; we then seal the capillary with 5-min epoxy (DevCon). After sealing, we can rehomogenize the sample at any time by agitating the magnetic wire with a magnetic stirrer. We maintain the temperature of the microscope stage and surrounding air at 25.0 ± 0.2 °C, yielding a buoyancy match between colloid and solvent that is better than $10^{-4}$. With the confocal microscope, we collect 3D stacks of 181 8-bit images, each 1,000 × 1,000 pixels, at 10 frames per second. Each image stack covers a volume of $60 \times 60 \times 60$ μm$^3$, taken from the centre of the sample at least 20 μm away from any capillary surface to minimize edge effects.

Although larger clusters persist in these samples, the confocal microscope can collect 3D stacks only a few times a minute, far too slowly to track monomers, dimers and other small clusters. Therefore, to ensure a broad sampling, after homogenization and equilibration for four hours, we collect 26 independent 3D image stacks within each fluid sample, separated by 100 μm laterally, using our automated confocal microscope[24]. To observe the evolution of gel samples, we homogenize and immediately start observations, collecting 3D stacks of the same sample volume every 50 s for the first 5,000 s, then every 1,000 s for the next 100,000 s. In each 3D stack, we determine the 3D position of each particle more than 1 μm from the boundary of the imaging volume using previously described image-processing software[24], and measure $\phi$ for each sample from these particle counts. In total, we collected half a terabyte of image data and determined the positions of ~$10^8$ particles. Our 3D reconstructions were rendered with Pixar's RenderMan.

**Simulations.** We perform simulations of $N = 10{,}000$ particles in a cubic box with periodic boundary conditions. For comparison to experimental samples with $c_p = 0$, we use the hard-sphere potential. For comparison to fluid samples with $c_p \geq 0$, we use three different attractive potential shapes, as shown in Fig. 2b: a square-well of width $0.04a$, an Asakura–Oosawa potential[33] of maximum width $0.08a$, and a generalized $2\alpha$-$\alpha$ Lennard–Jones potential with exponent $\alpha = 100$ (ref. 34). For the Asakura–Oosawa potential, we use Monte Carlo simulations[35]; for the hard-sphere and square-well potentials, a standard event-driven algorithm[36]; and for the Lennard–Jones potential, molecular dynamics[35]. In the latter cases, the system is at first equilibrated in the *NVT* ensemble, followed by a production run in the *NVE* ensemble, where 100 independent realizations are collected and analysed.

**Cluster mass distribution comparisons.** In particle configurations from both experiment and simulation, we define two particles as bonded if their centres are separated less than the bond distance $r_b$. All particles in a cluster share at least one bond with at least one other particle in the same cluster. Particles in one cluster share no bonds with particles in other clusters. Experimental uncertainties in particle locations arise from particle diffusion during confocal imaging, forcing the choice of $r_b$ to be slightly larger than its ideal value of the particle diameter $d = 2a$ plus the interaction range, for example, $1.08d$ for the previously described Asakura–Oosawa potential. We therefore set $r_b$ by matching the hard-sphere simulations to the sample with $c_p = 0$, fixing this value for all samples at $r_b = 1.16d$; $n(s)$ comparisons are independent of the particular choice of $r_b$, so long as a consistent definition is applied to both experiments and simulations. For each experimental sample, we ran the simulations at the same $\phi$. The least-squares procedure to match $n(s)$ from experiment and simulation equally weights all clusters.

**Static structure factor.** For fluid samples, we average the static structure factor $S(q) \equiv \left\langle \left| \sum_{j=1}^{N} \exp(i\mathbf{q}\cdot\mathbf{r}_j) \right|^2 \right\rangle \Big/ N$, where $\mathbf{r}_j$ are the coordinates of particle $j$, over the 26 independent configurations. For the gel samples, we follow a single configuration over time. We calculate $S(q)$ for all particles more than 4 μm away from all boundaries of the imaging volume to minimize edge effects, which, if present, would affect only the range $2qa \leq 0.2$. For the first moment $q_1(t) \equiv (\int_0^{q_c} S(q,t)q\mathrm{d}q)/(\int_0^{q_c} S(q,t)\mathrm{d}q)$, we select the cut-off value $2q_c a = 3$ to ensure the inclusion of all large wavelength contributions.

**Estimation of $\phi$ and $B_2^*$ for gel samples.** We extend the linear fit of the $U/k_BT$ versus $c_p$ for the fluid samples into the gel region at each $\phi$ to estimate $\tau \equiv 1/4(B_2^* - 1)$ for the gel samples shown in Fig. 4d. We estimate $\phi_g$, the internal volume fraction for spanning gel clusters, defined as those touching opposite faces of the cubic imaging volume, by measuring the free volume accessible to a spherical test particle of radius $a$. Splitting the imaging volume into a fine grid of cubes with edge length $l_c \ll a$, we place a test particle in each cube, and if no part of it intersects with spanning cluster particles, the volume occupied by the test particle is considered to be in the free volume. The fraction of sample volume not part of the free volume is considered to be the total cluster volume. The total volume of the particles within the cluster is their number times the volume per particle; dividing this by the total cluster volume yields $\phi_g$. We selected $l_c = 0.25a$, but the measured $\phi_g$ values do not depend on $l_c$ for values below ~$a/2$ and converge as expected for tests on standard structures, such as a cluster of the f.c.c. lattice, where $\phi \rightarrow 0.74$. This approach is strictly applicable only to structures, such as the present gels, where the solid phase is more dense at the scale of a single particle; our centrosymmetric interparticle attraction allows bond rotation without energy cost, thereby requiring multiple bonds for stable structures, leading to locally higher densities at the single-particle scale. By contrast, in the $\phi \rightarrow 0$ limit of DLCA, the permanent particle bonds are fixed and do not allow rotation, resulting in a more string-like local structure. For a straight line of spheres, our measure yields the analytic result $\phi = 4/(10 - \pi\sqrt{3}) \approx 0.88$, but is less meaningful in this regime.


31. Frisken, B. J. Revisiting the method of cumulants for the analysis of dynamic light-scattering data. *Appl. Opt.* **40**, 4087–4091 (2001).
32. Lekkerkerker, H. N. W., Poon, W. C. K., Pusey, P. N., Stroobants, A. & Warren, P. B. Phase behavior of colloid+polymer mixtures. *Europhys. Lett.* **20**, 559–564 (1992).
33. Asakura, S. & Oosawa, F. On interaction between two bodies immersed in a solution of macromolecules. *J. Chem. Phys.* **22**, 1255–1256 (1954).
34. Vliegenthart, G. A., Lodge, J. F. M. & Lekkerkerker, H. N. W. Strong weak and metastable liquids structural and dynamical aspects of the liquid state. *Physica A* **263**, 378–388 (1999).
35. Allen, M. P. & Tildesley, D. J. *Computer Simulation of Liquids* (Oxford Univ. Press, Oxford, UK, 1989).
36. Rapaport, D. C. *The Art of Molecular Dynamic Simulation* (Cambridge Univ. Press, Cambridge, UK, 1995).